Chemical Engineering Journal 99 (2004) 89–104

Chemical Engineering Journal

www.elsevier.com/locate/cej

Structural modelling for the dissolution of non-porous ores: dissolution with sporulation

Alessandra Adrover [a], Antonio Velardo [a], Massimiliano Giona [a,*], Stefano Cerbelli [a], Francesca Pagnanelli [b], Luigi Toro [b]

[a] *Dipartimento di Ingegneria Chimica, Facolta di Ingegneria, Universitá di Roma "La Sapienza", Via Eudossiana 18, 00184 Rome, Italy*
[b] *Dipartimento di Chimica, Universitá di Roma "La Sapienza", Piazzale Aldo Moro 5, 00185 Rome, Italy*

Received 3 July 2003; accepted 4 October 2003

Abstract

This article develops a structural model for the dissolution of non-porous ore particles, referred to as "sporulation" kinetics. This model is based on the assumption that the particulate can be modelled as an ensemble of reactive solid grains (e.g. metallic oxides) embedded into a solid matrix (gangue). The solid matrix may not be chemically inert with the result that, during the dissolution of the ore particle, the solid matrix "sporulates", i.e. grains of the reactive solid are progressively released from the ore particle into the liquid solution, due either to mechanical fragmentation or to chemical dissolution of the matrix itself. This model is applied in order to interpret the dissolution kinetics of manganiferous ores, which differs significantly from the corresponding kinetic behaviour of pure MnO_2 particles.

Keywords: Leaching; Intraparticle heterogeneity; Dissolution; Mineral processing

1. Introduction

Non-catalytic fluid–solid reactions are a class of industrially relevant operations whose structural properties of solid particles influence and modify the reaction evolution.

The overall evolution of the kinetics depends on several concurring processes: (i) the reaction kinetics sensu stricto and, specifically, the dependence of the dissolution rates on the concentration of fluid reactants; (ii) transport effects and mass-transfer limitations; (iii) the structural properties of solid particles; and (iv) the occurrence of mechanical/dissolution processes leading to particle fragmentation and break-up induced either by the mechanical stirring or by the dissolution kinetics itself [1,2]. The latter two effects depend on the polydispersity of the mixture, and influence the dynamics of the particle distribution function during the dissolution process.

Within the broad category of "structural properties of solid particles" several features may be identified, which can be further classified into several subcategories: (i) surface heterogeneities; (ii) particle ensemble properties; and (iii) intraparticle heterogeneity in the spatial distribution of the solid reactant within the solid pellet. Each of these properties leads to a specific modelling since it influences the overall reaction evolution in a different way.

Surface heterogeneity implies the occurrence of rough external surfaces induced, e.g. by the superposition and the intermingling of crystallites and crystalline planes. Surface heterogeneity can be modelled either by means of fractal concepts [3,4] or by modifying the shrinking-core model in order to account for the increase of the wetted surface in the external layer.

Particle ensemble properties refer to the occurrence of a spectrum of particle sizes. In the presence of a broad particle size distribution, the evolution of the reacting system can hardly be modelled by lumping together the particle ensemble and by considering an effective particle with an average radius. Indeed, the assumption of uniform particle size may induce severe kinetic misinterpretation of the kinetic process, leading to gross scale-up processes, in the presence of a broad distribution of particle radii [6–8]. This means that the particle ensemble should be described by means of a distribution function which is parameterised, e.g. with respect to the particle radius and thus leading to a population balance equation.

The third origin of heterogeneity refers to the spatial distribution of the reactive solid within the solid particle, made by an inert matrix, within which reactive grains are

* Corresponding author. Tel.: +39-06-445-85-892; fax: +39-06-445-85-339.
E-mail address: max@giona.ing.uniroma1.it (M. Giona).

1385-8947/$ – see front matter © 2003 Elsevier B.V. All rights reserved.
doi:10.1016/j.cej.2003.10.001

Nomenclature

$a(r_p)$	fragmentation rate
A_i	liquid reactant (A_1: glucose; A_2: sulphuric acid)
$b(r_p, r'_p)$	fragmentation kernel
c_i	liquid reactant concentration
$\tilde{c}_i$	dimensionless liquid reactant concentration ($=c_i/c_S$)
c_S	molar concentration of the solid reactant referred to the liquid solution volume V, see Eq. (37)
k_o	kinetic rate coefficient for the dissolution of the metal oxide
k_p	kinetic rate coefficient for the dissolution of the solid matrix
$m_o(\tilde{r}_o)$	weight distribution function of oxide grains within the ore particle ($m_o(\tilde{r}_o)\,d\tilde{r}_o$ is the weight fraction of oxide grains of radius in the range $[\tilde{r}_o, \tilde{r}_o + d\tilde{r}_o]$ embedded in the ore particle at time $t = 0$)
M	solid matrix (gangue)
$M_o(\tilde{r}_p)$	weight function of metal oxide embedded in the ore particle up to the radius $\tilde{r}_p$
M_p	overall particle mass
MW_p	average molecular weight of the ore particle
$n_o(r_o, t)$	distribution function of oxide grains in the liquid solution at time t ($n_o(r_o, t)\,dr_o$ is the number of oxide grains possessing radius between r_o and $r_o + dr_o$ at time t)
$n_p(r_p, t)$	distribution function of ore particles in the liquid solution at time t ($n_p(r_p, t)\,dr_p$ is the number of ore particles possessing radius between r_p and $r_p + dr_p$ at time t)
N_p	number of ore particles
$r_o(t)$	oxide grain radius at time t
$r_p(t)$	ore particle radius at time t ($R_p = r_p(t = 0)$)
S	solid reactant
t	time
T	temperature
$V_g(t)$	gangue volume within the ore particle at time t ($V_g^0 = V_g(t = 0)$)
$V_o(t)$	metal oxide volume within the ore particle at time t ($V_o^0 = V_o(t = 0)$)
$V_p(t)$	ore particle volume at time t ($V_p^0 = V_p(t = 0)$)
X	solid reactant conversion
Y	solid matrix (gangue) conversion

Greek letters

$\alpha(\tilde{r}_p)$	see Eq. (61)
β_o	dimensionless kinetic rate coefficient for the dissolution of the metal oxide
β_p	dimensionless kinetic rate coefficient for the dissolution of the solid matrix
Γ	see Eqs. (40) and (62)
ζ_i	parameter entering the distribution $\tilde{\nu}(\tilde{r}_o, \tilde{r}_p)$, see Eq. (49)
$\eta(\tau - \tau')$	unit step function
λ	see Eq. (70)
μ_i	stoichiometric coefficient of the dissolution reaction of the solid matrix (Eq. (6))
$\bar{\mu}_2$	see Eqs. (42), (45) and (69)
ν_i	stoichiometric coefficient of the dissolution reaction of the solid reactant (Eq. (1))
$\nu(r_o, r_p)$	distribution function of oxide grains within the ore particle ($\nu(r_o, r_p)4\pi r_p^2 dr_p dr_o$ is the number of oxide grains possessing radius in the range $[r_o, r_o + dr_o]$ and embedded in the volume $4\pi r_p^2 dr_p$ of the ore matrix)
ρ_g	gangue density
$\tilde{\rho}_g$	gangue molar density
ρ_o	oxide grain density
$\tilde{\rho}_o$	oxide grain molar density
ρ_p	ore particle density
$\tilde{\rho}_p$	ore particle molar density
τ	dimensionless time
ω	dissolution rate of pure reactant solid particles (Eq. (4))

Superscripts

av	spatial average
stoic	stoichiometric loading conditions
0	evaluated at time $t = 0$
$\sim$	dimensionless variable (unless otherwise explicitly stated)

embedded. Obviously, this situation cannot occur in the case of solid particles made of pure reactant. The modelling of this kind of heterogeneity, specifically oriented towards gas–solid non-catalytic reactions has been extensively investigated by Szekely et al. [9]. The approach envisaged by these authors led to the concept of *grain models*: structural models which account for the spatial distribution of solid reactant within the pellet.

The grain model, in its classical formulation, refers to porous particles in which the solid reactant, in the form of spherical grains, is embedded within an inert matrix which is permeable to the flow of gaseous reactants and products. Therefore, the non-uniform (radial) distribution of solid reactant modulates the interplay between intraparticle diffusion of gaseous reactants/products and the reaction occurring at the boundary of each grain. Grain models have been successfully applied to several gas–solid reactions of industrial interest (for a review see [9]).

For initially non-porous particles, the crackling core model proposed by Park and Levenspiel [10,11] for gas–solid reactions assumes that the reaction gas forces the particle to develop a system of cracks and fissures, resulting

in a grain material which is then easily penetrated by the reaction gas. Grains, generally assumed uniform in size, subsequently react via the shrinking-core model to the final product.

For what concerns liquid–solid systems, i.e. towards dissolution and leaching kinetics, intraparticle heterogeneity induces many different and complex phenomenologies and a structural model specifically suited for leaching kinetics should take into account the fact that intraparticle heterogeneity may also play a significant role in non-porous particles, due to dissolution/break-up of the solid matrix, thus exposing reactive grains to the liquid solution.

This article addresses a new model referred to as the sporulation model, which is based on the assumption that, during the dissolution/fragmentation of the ore particles, reactive grains are released in the liquid phase.

This article is organised as follows. Section 2 attempts a classification of structural models for non-porous particles in leaching processes. Section 3 describes the experimental set-up and the experimental observations on the dissolution of manganiferous ores, motivating the formulation of the sporulation model. A thorough description of model assumptions and of its mathematical setting is developed in Section 4. Section 5 analyses the typical features of the sporulation model through representative numerical simulations. In Section 6, the sporulation model is generalised, to address the case of a non-uniform radial distribution of reactive solid within the ore particle. Indeed, Sections 4–6 are devoted to present, in a classical framework for chemical reaction engineering, a general approach towards sporulation modelling, by discussing first the homogeneous case and then by including the effect of polydispersity of the solid mixture, of the ore particle fragmentation and of a non-uniform radial distribution of solid reactant within the ore particle. Section 7 applies the sporulation model to the dissolution of manganiferous ores.

2. Structural models for the dissolution of non-porous particles

This section attempts to classify the different structural models able to describe the evolution of non-catalytic liquid–solid reactions in the presence of non-porous pellets, by focusing on the influence of ensemble and intraparticle heterogeneity.

Let us assume that solid pellets contain a reactive species S which reacts with the liquid reactants A_i $(i = 1, 2)$ to yield the product P which dissolves into the liquid phase:

$$S\,(\mathrm{s}) + \nu_1 A_1\,(\mathrm{f}) + \nu_2 A_2\,(\mathrm{f}) \rightarrow P\,(\mathrm{f}), \tag{1}$$

where ν_i $(i = 1, 2)$ are the stoichiometric coefficients. The non-porous nature of the solid pellet implies that fluid reactants do not penetrate within the solid particle, and consequently reaction (1) occurs exclusively at the external boundary of the particles.

Mathematical models can be conveniently subdivided into two main categories, depending on the type of heterogeneity that is accounted for.

2.1. Ensemble heterogeneity

Let us first consider the case of pure reactive solids. In this case, ensemble heterogeneity plays a leading role in the evolution of the reaction, with the result that an accurate model combines the kinetic information (rate of dissolution associated with Eq. (1)) and the mathematical description of the possible fragmentation process, which in turn leads to a break-up of the larger particles into smaller ones. This can be achieved, within the framework of population balances, by encompassing the physical processes affecting the overall reaction, i.e.: (i) the reaction kinetics sensu stricto and, more specifically, the dependence of the dissolution rates on the concentration of fluid reactants; (ii) transport effects and mass-transfer limitations; (iii) the structural properties of particle ensembles expressed by the particle distribution function with respect to the geometric radius [6,7,12–15]; and (iv) the mechanical/dissolution effects leading to particle fragmentation and break-up induced either by the mechanical stirring or by the dissolution kinetics itself [1,2].

Let $n(r, t)$ be the particle distribution function with respect to the radius r, so that $n(r, t)\,\mathrm{d}r$ is the number of solid particles possessing, at time t, radius between r and $r + \mathrm{d}r$. For batch dissolution, under the assumption of perfect stirring, the population balance equation reads as:

$$\frac{\partial n(r,t)}{\partial t} + \frac{\partial}{\partial r}\{\omega[r, N_3(t)]n(r,t)\} = -a(r)n(r,t) + \int_0^\infty a(\rho)b(r;\rho)n(\rho,t)\,\mathrm{d}\rho. \tag{2}$$

The function $a(r)$ is the fragmentation rate, and $b(r; \rho)$ the number of fragments of radius r generated from a particle of radius ρ. By definition, the fragmentation kernel $b(r; \rho)$ satisfies the constraint $b(r; \rho) = 0$, for $\rho < r$, and the mass-conservation condition [1,2]:

$$\rho^3 = \int_0^\rho r^3 b(r;\rho)\,\mathrm{d}r. \tag{3}$$

Expressions for the rate of fragmentation and for the kernel $b(r; \rho)$ can be found in the literature [1,16].

The term $\omega[r, N_3(t)]$ is the dissolution rate, that is:

$$\frac{\mathrm{d}r}{\mathrm{d}t} = \omega[r, N_3(t)], \tag{4}$$

which, in the most general setting, is a non-linear integral functional of the distribution function $n(r, t)$, since it may depend explicitly on its third-order moment:

$$N_3(t) = \int_0^\infty r^3 n(r,t)\,\mathrm{d}r. \tag{5}$$

2.2. Intraparticle heterogeneity

Intraparticle heterogeneity means that solid particles are not exclusively composed by the reactant S, and indeed the solid reactant is embedded within a solid matrix formed by chemical species not participating in the reaction (1). This is typical in mineral processing and ore leaching. The solid matrix M may not be chemically inert. Indeed, it may participate in other dissolution side reactions, such as:

$$M\,(\mathrm{s}) + \mu_2 A_2\,(\mathrm{f}) + \mu_3 A_3\,(\mathrm{f}) \rightarrow W(\mathrm{f}), \tag{6}$$

in which one of the fluid species A_2, involved in the main dissolution reaction (1), takes part. In Eq. (6), μ_i $(i = 2, 3)$ are the stoichiometric coefficients associated with this side reaction, and W (for "waste") is the reaction product.

From the setting of the problem described earlier, it is clear that the central issue in the development of structural models which account explicitly for intraparticle heterogeneity resides in the interplay between the dissolution kinetics of the solid reactant S and the dissolution/fragmentation of the matrix M, as a consequence of which reactive solid grains become exposed to the liquid phase. It should be observed that a quantitative mathematical description for this phenomenon in the presence of non-porous particles is conceptually different from the grain models developed by Szekely et al. for gas–solid reactions of porous particles, in which intraparticle heterogeneity was essentially associated with intraparticle diffusion.

The sporulation model, which will be developed in the following sections, is specifically suited to accounting for the intraparticle heterogeneity, by describing the interplay between the dissolution of the solid reactant and the dissolution of the matrix.

Model development is preceded by a short description of the physical problems and experimental results motivating the basic model assumptions.

3. MNO_2 dissolution: experimental observations

As a test case let us consider the dissolution kinetics of manganiferous ores. The recovery of metals and particularly of manganese from mineral ores is an important industrial issue. A series of hydrometallurgical processes have been developed both with and without reducing agents. One of the processes developed makes use of sacchariferous reducing agents (glucose in the present analysis). Recently, bioleaching of manganese by iron-oxidising bacteria has been addressed [17,18]. Leaching kinetics of manganiferous ore (pyrolusite) have been considered by several authors [19,20].

Manganese extraction using carbohydrates as reducing agents consists of a complex network of chemical reactions involving partially oxidised products derived from carbohydrate degradation in acidic media. The manifold of intermediates and their variability with carbohydrate sources led to the formulation of a preliminary kinetic model considering the following overall chemical reaction [21]:

$$\mathrm{C_6H_{12}O_6} + 12\mathrm{MnO_2} + 24\mathrm{H^+} = 6\mathrm{CO_2} + 12\mathrm{Mn^{2+}} + 18\mathrm{H_2O}, \tag{7}$$

thus overlooking all possible intermediate products and reactions. A shrinking-core model with a variable activation energy (the activation energy is assumed to be a function of the overall conversion), was developed in [22]. This model can be fitted successfully to the experimental data of manganese ore leaching obtained at different operating conditions [23], although the functional form of the dissolution rate is rather complex and the model contains many adjustable parameters.

3.1. Materials and methods

The manganiferous ore considered in this study comes from an Italian mine located in North Latium and is primarily made up of manganese as pyrolusite (MnO_2) in an orthoclase matrix ($KAlSi_3O_8$), as shown from XRD analysis reported in other studies [24]. Manganese content was determined by ore dissolution which was performed in a microwave digestion unit (MLS 1200 MEGA high performance microwave) using 0.1 g of solid, 6 ml HCl (37% RPE Carlo Erba Reagents) and 2 ml HF (40% RPE Carlo Erba Reagents): the final solution was analysed by an inductively coupled plasma spectrophotometer (ICP) to determine the weight percent of the main elements present in the ore [24]. Leaching tests of manganiferous ore were performed in cylindrical jacketed vessels (borosilicate glass, 200 ml) with round bottom and upper opening for sample collection. Each leaching test was carried out under magnetic stirring and at selected constant temperature (30, 50 and 70 °C) using a digital bath with a circulating pump (LT5 IKA Labortechnik). The reductive leaching process was carried out in sulphuric acid media (H_2SO_4 96% ISO for analysis, Carlo Erba Reagents) using glucose (α-D-glucose anhydrous, 96%, Sigma–Aldrich) as a reducing agent according to the global stoichiometry of the reaction reported in Eq. (7).

We made use of a small reactor in order to ensure a good level of homogeneity of the liquid–solid solution with the simple use of a magnetic stirrer. Different experiments have been performed for increasing stirring speeds confirming that : (i) a good level of homogeneity of the liquid–solid solution is attained; and (ii) mechanical fragmentation effects are indeed negligible.

Leaching test were performed in different loading conditions considering the global reaction reported in Eq. (7) as a reference: in particular, leaching tests at different temperatures were performed in stoichiometric conditions of both acid and glucose, with an excess of acid and stoichiometric glucose, with stoichiometric acid and an excess of glucose and with stoichiometric acid in the absence of glucose (see Section 3.2 for a detailed discussion of the meaning

of the different loading conditions). During each leaching test different samples of both leach liquor and solid residual ore were collected to determine Mn extraction and particle size distribution respectively. Solid–liquid separation was performed by centrifugation (Chermle Z380) for 10 min at 8000 min^{-1}. Liquid samples were diluted with a HNO_3 solution in distilled water (0.01 M) and then analysed by ICP to determine Mn concentration. A laser diffraction equipment (Helos Sympatec, FR Germany) was used to determine the particle size distribution in the liquid phase of different ore samples which were collected during the leaching and then washed and stored in distilled water. Higher solid concentrations in the liquid suspension were employed in the experiments mainly devoted to investigate the time evolution of particle size distribution. All the experiments have been repeated three times in order to ensure the reproducibility of the data and the negligible influence of sample collection.

Experiments have been also performed with MnO_2 particles, purchased from Sigma–Aldrich (60–230 mesh, purity 99%) at 90 °C. Below 90 °C, the conversion achieved after 40 h is too low to have any practical interest.

3.2. Manganiferous ores versus pure MnO_2 dissolution

A thorough understanding of ore leaching kinetics is made complex by the structural properties of the particles and by the spatial distribution of MnO_2 crystallites within the amorphous solid matrix. In order to achieve a better understanding of the kinetics underlying the reaction described by Eq. (7), it is useful to consider the leaching process of pure MnO_2 particles.

By referring to Eq. (1), let us indicate glucose with A_1 and sulphuric acid with A_2, so that the stoichiometric coefficients are $\nu_1 = 1/12$ and $\nu_2 = 1$.

Velardo et al. [5] recently analysed dissolution kinetics of pure MnO_2 in acidic medium and in the presence of glucose as the reducing agent, showing that: (i) the kinetic rate does not depend significantly on the concentration of sulphuric acid; and (ii) the dissolution rate ω entering the balance equation can be expressed by means of the following expression:

$$\omega = -k_o c_1^{n_1}, \tag{8}$$

where c_1 is glucose concentration, k_o the rate constant and $n_1 = 1.2$. The fact that the dissolution rate is practically unaffected by the sulphuric acid can be observed from the data depicted in Fig. 1a which shows the experimental results for the conversion–time curves $(1 - X(t))^{1/3}$ versus t at $T = 90$ °C for several loading conditions:[1] under stoichiometric loading for glucose ($\tilde{c}_1(0) = \nu_1$), by keeping sulphuric acid under stoichiometric loading ($\tilde{c}_2(0) = \nu_2$), and in the case of a 30% surplus ($\tilde{c}_2(0) = 1.3\nu_2$) (dataset (a)); for 50% glucose surplus ($\tilde{c}_1(0) = 1.5\nu_1$), under stoichiometric ($\tilde{c}_2(0) = \nu_2$), and 50% surplus ($\tilde{c}_2(0) = 1.5\nu_2$) of sulphuric acid (dataset (b)).

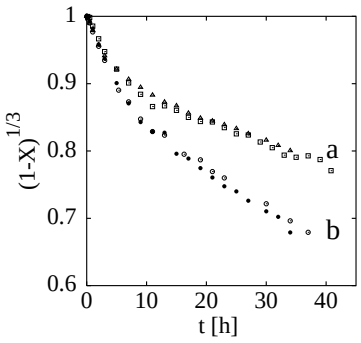

Fig. 1. Influence of sulphuric acid concentration on the dissolution of pure MnO_2 particles. Conversion–time curves $(1 - X(t))^{1/3}$ vs. t (h). Set (a) refers to stoichiometric loading conditions of glucose $\tilde{c}_1(0) = \nu_1$: (□) stoichiometric loading of sulphuric acid $\tilde{c}_2(0) = \nu_2$; (△) 30% surplus of sulphuric acid $\tilde{c}_2(0) = 1.3\nu_2$. Set (b) refers to 50% glucose surplus $\tilde{c}_1(0) = 1.5\nu_1$: (●) stoichiometric loading of sulphuric acid $\tilde{c}_2(0) = \nu_2$; (○) 50% surplus of sulphuric acid $\tilde{c}_2(0) = 1.5\nu_2$.

A surplus of sulphuric acid, the other operating parameters being fixed, does not increase the overall conversion so that, for pure MnO_2 particles, it can be reasonably assumed that the dissolution rate is independent of the concentration c_2 of H_2SO_4. The data of pure MnO_2 dissolution refers to the temperature $T = 90$ °C, since below 90°C, the conversion achieved after 40 h is too low to have any practical interest.

Let us now consider the dissolution kinetics of manganiferous ores, made by MnO_2 grains (S, weight fraction 0.15) embedded in the solid matrix (M, weight fraction 0.85). Let us indicate the conversion of MnO_2 grains with $X(t)$.

The overall conversion–time curves $X(t)$ versus t are depicted in Fig. 2A–C, for three different values of the temperature $T = 30$, 50, and 70 °C (curves (a)–(c), respectively) and for different loading conditions. Fig. 2A refers to the loading condition:[2] $\tilde{c}_1(0) = \nu_1$ and $\tilde{c}_2(0) = \nu_2$, while Fig. 2B refers to $\tilde{c}_1(0) = \nu_1$ and $\tilde{c}_2(0) = 1.3\nu_2$.

The results depicted in these figures lead to the following observations: (i) the dissolution rate increases monotonically with temperature (Fig. 2A); (ii) the conversion–time curves saturate towards a limiting value $X_s \simeq 0.83 < 1$ that does not depend on temperature (Fig. 2A); (iii) the dissolution

[1] The loading conditions of fluid reactants can be expressed in terms of the dimensionless concentrations $\tilde{c}_1(0) = c_1(0)/c_S$ and $\tilde{c}_2(0) = c_2(0)/c_S$, where $c_1(0)$ and $c_2(0)$ are fluid reactant concentrations at time $t = 0$ and $c_S = n_S/V$ is the molar concentration of the solid reactant referred to the liquid solution volume V. In the case of pure MnO_2 particles, fluid reactant concentrations evolve in time according with the equations:

$$\tilde{c}_1(t) = \frac{c_1(t)}{c_S} = \tilde{c}_1(0) - \nu_1 X, \qquad \tilde{c}_2(t) = \frac{c_2(t)}{c_S} = \tilde{c}_2(0) - \nu_2 X,$$

where X is the solid reactant conversion. Therefore, in the case of pure MnO_2 particles, for stoichiometric loading condition for the fluid reactant A_1 (or equivalently for A_2) we mean $\tilde{c}_1(0) = \tilde{c}_1^{stoic} = \nu_1$, so that $\tilde{c}_1(t) \to 0$ for $X \to 0$. The concept of "surplus" of a fluid reactant is referred to its molar content with respect to the stoichiometric loading, so that a loading condition of 30% surplus of glucose means that $\tilde{c}_1(0) = 1.3\tilde{c}_1^{stoic} = 1.3\nu_1$.

[2] In the case of ore particles, the stoichiometric loading condition for A_1 = glucose corresponds to $\tilde{c}_1(0) = \nu_1$, while for A_2 = sulphuric acid corresponds to $\tilde{c}_2(0) = \nu_2 + \tilde{\mu}_2$ (see Section 5).

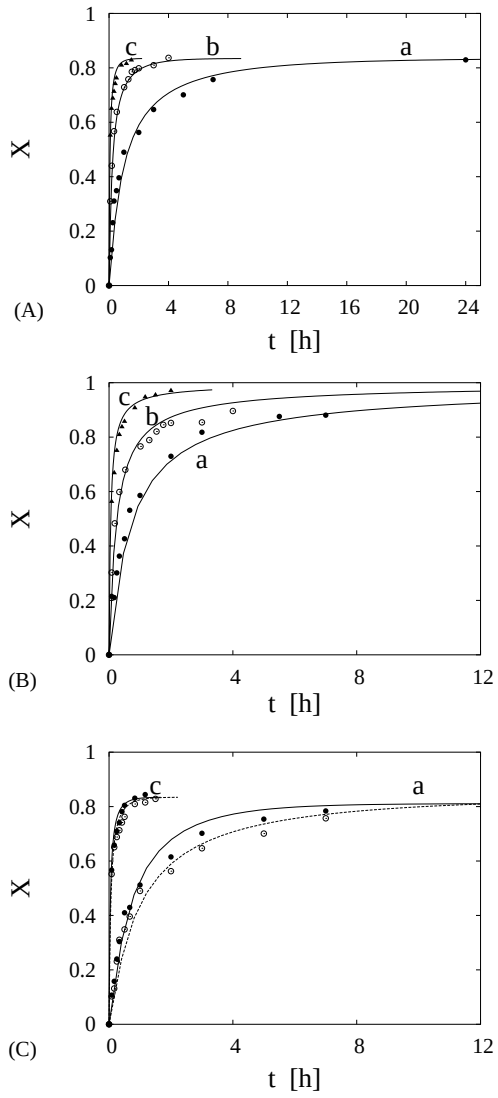

Fig. 2. Conversion–time curves $X(t)$ vs. t (h) for manganiferous ore particles for three different values of the temperature $T = 30$, 50, and 70 °C (curves (a)–(c), respectively) and for different loading conditions. Continuous and dotted lines are the predictions of the "homogeneous" sporulation model (see Section 7). (A) Loading conditions $\tilde{c}_1(0) = \nu_1$ and $\tilde{c}_2(0) = \nu_2$. (B) Loading conditions $\tilde{c}_1(0) = \nu_1$ and $\tilde{c}_2(0) = 1.3\nu_2$. (C) Open circles and dotted lines refer to the loading conditions $\tilde{c}_1(0) = \nu_1$ and $\tilde{c}_2(0) = \nu_2$; open circles and continuous lines refer to the loading conditions $\tilde{c}_1(0) = 1.3\nu_1$ and $\tilde{c}_2(0) = \nu_2$.

rate increases monotonically with the concentration of the sulphuric acid (Fig. 2B); and (iv) after 8 h, for $\tilde{c}_2(0) = 1.3\nu_2$, the conversion is already significantly higher than the limiting value X_s, obtained for $\tilde{c}_2(0) = \nu_2$ (Fig. 2B).

These experimental observations indicate that a chemical dissolution of the solid matrix (gangue) occurs for manganiferous ores due to the presence of sulphuric acid, and this phenomenon speeds the leaching process up significantly. In point of fact, the chemical dissolution of the solid matrix, together with mechanical stirring, enhances the release of oxide reactive grains from the matrix into the liquid solution.

In other words, sulphuric acid acts as a fluid reactant for the dissolution of both oxide grains and the solid matrix. For this reason, in the case of manganiferous ore particles, the sulphuric acid loading condition $\tilde{c}_2(0) = \nu_2$ does not represent the "stoichiometric" loading, because of the occurrence of the side reaction of solid matrix dissolution, which consumes sulphuric acid. That is the reason why, for $\tilde{c}_2(0) = \nu_2$, the oxide grain conversion saturates towards a limiting value $X_s < 1$.

The fact that the sulphuric acid is the limiting reactant, is confirmed by Fig. 2C, which depicts the influence of initial glucose concentration $\tilde{c}_1(0)$. Fig. 2C shows the overall

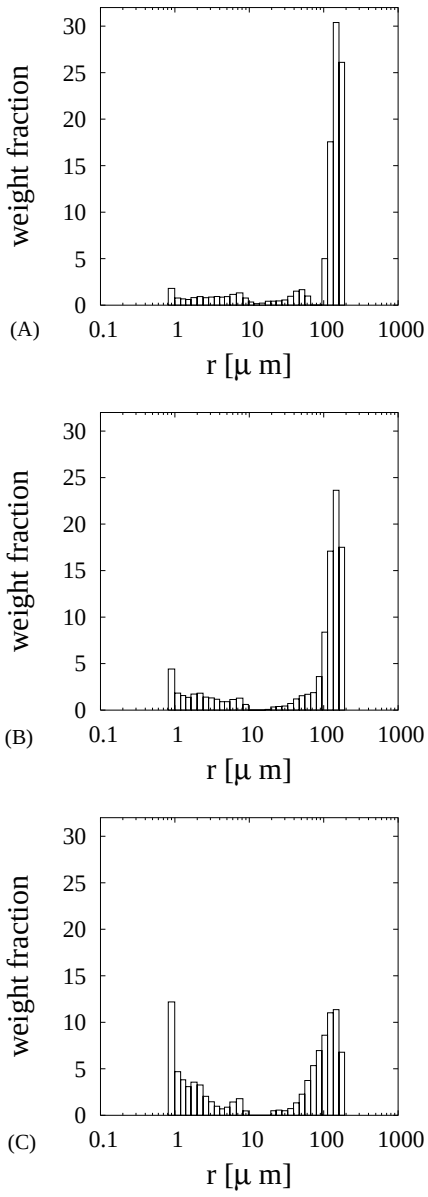

Fig. 3. Granulometric data for a leaching experiment of manganiferous ores in the absence of the reducing agent (glucose) for $T = 90$ °C and $\tilde{c}_2(0) = \nu_2$. Histograms show the weight fraction of particles possessing radius between r and $r + \Delta r$. Parts (A)–(C) refer to three different time instants, $t = 0$, 8 and 24 h, respectively.

conversion–time curves $X(t)$ versus t for two different values of the temperature $T = 30$, and 70 °C, and for different loading conditions. Open circles refer to stoichiometric loading condition for glucose $\tilde{c}_1(0) = \nu_1$ and $\tilde{c}_2(0) = \nu_2$. Filled circles refer to a 30% surplus of glucose $\tilde{c}_1(0) = 1.3\nu_1$ and $\tilde{c}_2(0) = \nu_2$. As can be observed, the dissolution rate slightly increases for increasing values of $\tilde{c}_1(0)$, but the saturation value of the conversion is practically unaffected by the glucose surplus. This confirms that glucose is not a limiting reactant.

The fact that the solid matrix undergoes a dissolution process is confirmed by granulometric data reported in Fig. 3, showing the particle weight fraction possessing radii between r and $r + \Delta r$, at three different time instants, $t = 0, 8, 24$ h. The granulometric data depicted in Fig. 3 refer to an experimental run in the absence of glucose and in the presence of the sulphuric acid. In the absence of the reducing agent (glucose) oxide grains do not dissolve and the time evolution of the particle distribution function (the weight fraction of particles characterised by smaller radii is increasing in time) is exclusively due to the dissolution/fragmentation of the solid matrix in the presence of sulphuric acid and mechanical stirring.

Different experiments, performed for increasing stirring speeds (not reported here), support the idea that fragmentation effects are indeed negligible with respect to solid matrix dissolution. No agglomeration or coating of larger particles can be hypothesised from the analysis of granulometric data.

4. Sporulation kinetics: model description

The experimental results depicted in Figs. 1 and 2A–C, indicate that the leaching process of manganiferous ores is significantly more efficient than that of pure MnO_2 particles. The difference is at least one order of magnitude in the time-scales: for a given conversion, say $X = 0.5$, it lasts more than 40 h for the pure mineral while it takes about 1 h for the ore. The comparison is kinetically fair, since both mineral and pure MnO_2 particles possess approximately the same granulometry. Moreover, granulometric data for an experimental run in the absence of glucose (Fig. 3) shows that ore particles undergo dissolution even in the absence of oxide grain dissolution.

The structural model discussed further, and referred to as *sporulation model*, is grounded on these experimental observations. In the light of the case study discussed in Section 2, we will use the wording “metallic oxide”, or “oxide” to indicate the reactive solid S, undergoing dissolution.

The mechanism underlying the sporulation model is depicted in Fig. 4. The ore particle contains smaller grains of the metal oxide that, due to dissolution/fragmentation kinetics of the solid matrix (gangue), are progressively released into the liquid phase. This implies that the sporulation model explicitly considers the interplay between oxide and gangue dissolution, by assuming that the dominant phenomenon controlling the process is the release of oxide grains into the liquid phase.

The sporulative release of solid grains within the liquid phase increases the wetted surface of the solid reactant S exposed to the liquid, thus enhancing the dissolution process. Ore particles and oxide grains are assumed to be spherical.

In order to simplify the treatment, the ore particle density ρ_p, and consequently the particle molar density $\bar{\rho}_p = \rho_p/MW_p$, is assumed to be constant during the dissolution process. This implies that the metal oxide is uniformly distributed within the solid matrix. The more general case of a non-uniform radial distribution of metal oxide within the matrix is addressed in Section 6.

Following Eq. (6), the dissolution of the ore matrix M can be expressed by the equation:

$$\bar{\rho}_p \frac{dV_p}{dt} = -k_p(T) g_p(c_2, c_3) S_p, \tag{9}$$

where V_p and S_p are the particle volume and particle surface, respectively, k_p the kinetic rate coefficient (which may depend on temperature T) and g_p a function of the concentrations c_2 and c_3 of the reacting species A_2 and A_3 within the liquid solution. The assumption of sphericity leads to:

$$\frac{dr_p}{dt} = -\beta_p(T) g_p(c_2, c_3), \tag{10}$$

where $\beta_p = k_p/\bar{\rho}_p$, and r_p is the particle radius. Likewise, the dissolution kinetics for the solid reactant S (oxide grain), according to Eq. (1), reads as:

$$\frac{dr_o}{dt} = -\beta_o(T) g_o(c_1, c_2), \tag{11}$$

where r_o is the oxide grain radius, $\beta_o = k_o/\bar{\rho}_o$, $k_o(T)$ the kinetic coefficient of the dissolution rate of the metal oxide, and $g_o(c_1, c_2)$ a function of the concentrations c_1 and c_2 of the reacting species A_1 and A_2 in the liquid solution.

The distribution of oxide grains within the ore particle is described by the function $\nu(r_o, r_p)$ representing the number of oxide grains per unit radius r_o and per unit volume of the ore particle, i.e. $\nu(r_o, r_p) 4\pi r_p^2 dr_p dr_o$ is the number of oxide grains possessing a radius in the range $[r_o, r_o + dr_o]$ and embedded in the volume $4\pi r_p^2 dr_p$ of the ore matrix.

Let $n_o(r_o, t)$ be the number of oxide grains per unit radius r_o in the liquid solution, so that $n_o(r_o, t)\, dr_o$ is the number of oxide grains possessing a radius between r_o and $r_o + dr_o$. Two cases should be discussed separately, depending on whether ensemble heterogeneity (referred to as the granulometric distribution of ore particles) is accounted for. Let us first consider the case of a uniform ensemble of ore particles, possessing the same initial radius R_p.

The evolution equation for $n_o(r_o, t)$ is simply given by the population balance:

$$\frac{\partial n_o}{\partial t} - \frac{\partial[\beta_o g_o n_o]}{\partial r_o} = -N_p \frac{dV_p}{dt} \nu(r_o, r_p) = N_p \beta_p g_p S_p \nu(r_o, r_p), \tag{12}$$

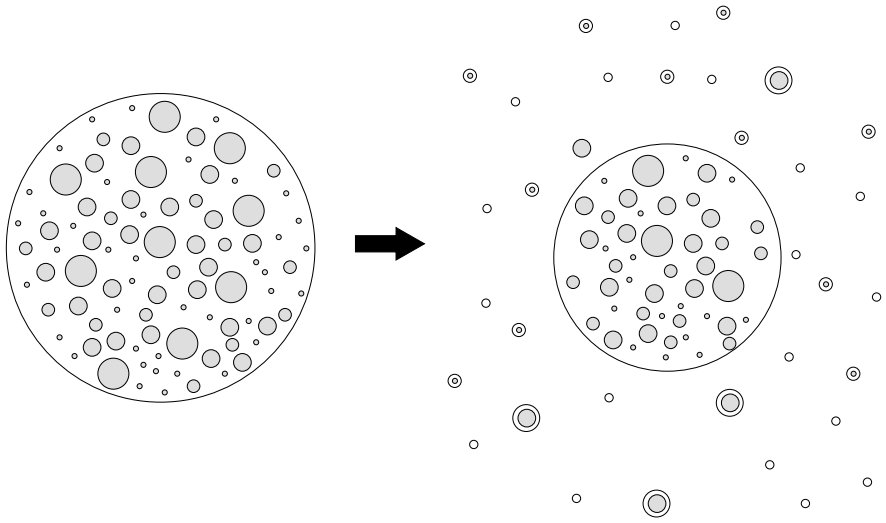

Fig. 4. Schematic representation of the "release" mechanisms of oxide grains from the ore particle into the liquid solution, characterising the sporulation model.

where N_p is the number of ore particles:

$$N_p = \frac{M_p}{\rho_p V_p^0}, \tag{13}$$

M_p the overall particle mass, and $V_p^0 = 4\pi R_p^3/3$ in the initial particle volume. Eqs. (10) and (12) define the sporulation model in the case of a uniform ore-particle mixture. The initial condition for $n_o(r_o, t)$ can be assumed as follows:

$$n_o(r_o, 0) = 0, \quad \text{for all } r_o, \tag{14}$$

which implies that no oxide particles are dispersed within the liquid phase at the beginning of the process.

In the case of a polydisperse mixture of solid particles, it is necessary to introduce a distribution function $n_p(r_p, t)$ representing the number of ore particles per unit radius r_p, so that:

$$N_p(t) = \int_0^\infty n_p(r_p, t)\, dr_p, \tag{15}$$

is the number of ore particles at time t. The distribution function $n_p(r_p, t)$ satisfies the balance equation:

$$\frac{\partial n_p}{\partial t} - \frac{\partial[\beta_p g_p n_p]}{\partial r_p} = 0, \tag{16}$$

starting from a given initial distribution $n_p(r_p, 0) = n_p^0(r_p)$. Eq. (16) is a population balance accounting exclusively for the chemical dissolution of the ore particles. In the presence of significant ore particle fragmentation, Eq. (16) modifies as follows:

$$\frac{\partial n_p}{\partial t} - \frac{\partial[\beta_p g_p n_p]}{\partial r_p} = -a(r_p) n_p + \int_0^\infty a(r_p') b(r_p, r_p') n_p(r_p', t)\, dr_p', \tag{17}$$

where $a(r_p)$ is the fragmentation rate and $b(r_p, r_p')$ the fragmentation kernel. Unless otherwise stated, we assume here that fragmentation effects due to mechanical stirring and abrasion are negligible so that Eq. (16) is the population balance for $n_p(r_p, t)$.

The inclusion of ensemble heterogeneity within the sporulation model forces to modify the population balance Eq. (12) for $n_o(r_o, t)$ accordingly, and the result is the following equation:

$$\frac{\partial n_o}{\partial t} - \frac{\partial[\beta_o g_o n_o]}{\partial r_o} = \int_0^\infty n_p(r_p', t) \beta_p g_p 4\pi (r_p')^2 \nu(r_o, r_p')\, dr_p'. \tag{18}$$

In the case of a homogeneous ore particle population:

$$n_p(r_p', t) = \delta(r_p' - r_p(t)), \tag{19}$$

where $r_p(t)$ is the solution of Eq. (10), and Eq. (18) reduces to Eq. (12). This article mainly addresses the influence of intraparticle heterogeneity and its description by means of the sporulation model proposed. Consequently, we will consider the case of a homogeneous ore particle distribution even though the inclusion of ensemble heterogeneity does not modify the fundamental architecture of the model as it can be shown by Eq. (16).

The functions and coefficients characterising the sporulation model are not completely arbitrary since their functional form and value should be consistent with the overall mass balance. The assessment of the overall mass balance induces quantitative constraints on the function $\nu(r_o, r_p)$. Firstly, it is reasonable to assume that:

$$\nu(r_o, r_p) = 0, \quad \text{for } r_o > r_p, \tag{20}$$

since an ore particle cannot inglobe an oxide grain of larger radius.

The physical constraint on $\nu(r_o, r_p)$ is obtained by enforcing that the initial mass of an ore particle $\rho_p V_p^0$ equals the mass of the oxide grains and the mass of the matrix, that is:

$$\rho_p V_p^0 = \rho_o V_o^0 + \rho_g V_g^0 = (\rho_o - \rho_g)\, V_o^0 + \rho_g V_p^0, \tag{21}$$

where ρ_o and ρ_g are oxide and gangue (matrix) densities, and V_o^0, V_g^0 the oxide and gangue volumes within the initial ore particle. From physical arguments, the densities ρ_o, ρ_g and ρ_p satisfy the following inequality:

$$\rho_g < \rho_p < \rho_o. \tag{22}$$

Eq. (21) can be reformulated as follows:

$$\frac{\rho_p - \rho_g}{\rho_o - \rho_g} V_p^0 = V_o^0 = \int_0^{R_p} 4\pi (r_p')^2 \, dr_p \int_0^{r_p'} \nu(r_o, r_p') \frac{4}{3}\pi r_o^3 \, dr_o, \tag{23}$$

which is an integral constraint on $\nu(r_o, r_p)$.

It is important to observe that it is possible to derive another more strict inequality for $\nu(r_o, r_p)$ by assuming the "homogeneity hypothesis", that is, during the dissolution process of the ore particles, the particle density ρ_p remains constant.

Under this hypothesis Eq. (21) can be extended to any time instant t, so that:

$$\frac{V_o(t)}{V_p(t)} = \frac{V_o^0}{V_p^0} = \frac{\rho_p - \rho_g}{\rho_o - \rho_g} \Rightarrow (\rho_p - \rho_g) V_p(t) = (\rho_o - \rho_g) V_o(t), \tag{24}$$

where $V_o(t)$ is the total volume of oxide grains embedded in the ore particle at time t when the ore particle volume is $V_p(t) = (4/3)\pi r_p^3(t)$. Eq. (24) can be further rearranged, by replacing $V_o(t)$ with its integral expression in which $\nu(r_o, r_p)$ enters explicitly:

$$(\rho_p - \rho_g) \int_0^{r_p(t)} 4\pi (r_p')^2 \, dr_p' = (\rho_o - \rho_g) \int_0^{r_p(t)} 4\pi (r_p')^2 \, dr_p' \int_0^{r_p'} \nu(r_o, r_p')(4/3)\pi r_o^3 \, dr_o, \tag{25}$$

i.e.

$$\int_0^{r_p(t)} 4\pi (r_p')^2 \times \left[(\rho_p - \rho_g) - (\rho_o - \rho_g) \int_0^{r_p'} \nu(r_o, r_p') \frac{4}{3}\pi r_o^3 \, dr_o \right] dr_p' = 0. \tag{26}$$

Since Eq. (26) should hold true for any time instant, i.e. for any $r_p(t)$, it follows that:

$$\int_0^{r_p(t)} \nu(r_o, r_p) \frac{4}{3}\pi r_o^3 \, dr_o = \frac{\rho_p - \rho_g}{\rho_o - \rho_g}. \tag{27}$$

It is important to observe that while Eq. (23) is an integral condition deriving exclusively from a material balance, Eq. (27) derives from the physical assumption of homogeneity.

In Section 5, we enforce Eq. (27), that is the "homogeneous constraint", to address the salient features of the sporulation model. The more general case in which the effective particle density may change during the dissolution process, is addressed in Section 6.

Let us conclude this presentation of the sporulation model by considering the explicit expression for the overall conversions X and Y of the main reactant S (i.e. of the metallic oxide) and of the solid matrix (gangue), respectively. The metal oxide conversion $X(t)$ at any time t is given by:

$$X(t) = 1 - [\text{fraction of oxide at time } t \text{ embedded within the ore particle}] - [\text{fraction of oxide at time } t \text{ contained in the released grains}], \tag{28}$$

so that $X(t)$ attains the form:

$$X(t) = 1 - \frac{V_o(t)}{V_o^0} - \frac{\int_0^{R_p} n_o(r_o, t) \frac{4}{3}\pi r_o^3 \, dr_o}{V_o^0}. \tag{29}$$

Analogously, the conversion Y of the solid matrix attains the form:

$$Y = 1 - \frac{V_p(t) - V_o(t)}{V_p^0 - V_o^0}. \tag{30}$$

The generalisation of Eqs. (29) and (30) to a polydisperse mixture of ore particles is straightforward.

In the case of ρ_p is constant during the dissolution process, Eq. (24) holds true so that:

$$X(t) = 1 - \frac{r_p^3(t)}{R_p^3} - \frac{\int_0^{R_p} n_o(r_o, t)(4/3)\pi r_o^3 \, dr_o}{V_o^0}, \quad Y = 1 - \frac{r_p^3(t)}{R_p^3}. \tag{31}$$

The potentialities of the sporulation model are discussed in detail in Section 5 where the "homogeneous" sporulation model is compared with the classical shrinking-core model in the case of zero- and first-order dissolution kinetics.

5. Model analysis and simulations

Without loss of generality, we consider the simplified reaction scheme:

$$S\,(\mathrm{s}) + \nu_1 A_1\,(\mathrm{f}) + \nu_2 A_2\,(\mathrm{f}) \rightarrow P\,(\mathrm{f}), \tag{32}$$

$$M\,(\mathrm{s}) + \mu_2 A_2\,(\mathrm{f}) \rightarrow W\,(\mathrm{f}), \tag{33}$$

with the functional dependencies of the rate coefficients:

$$g_p(c_2) = c_2^{n_2}, \qquad g_o(c_1, c_2) = c_1^{n_1}, \tag{34}$$

i.e. we assume that the reaction rate of oxide grains $k_o g_o(c_1)$ is independent on the concentration of the fluid species A_2, which is responsible for the dissolution of the solid matrix accounted for by the reaction rate $k_p g_p(c_2)$.

By introducing the dimensionless variables and parameters:[3]

$$\tilde{r}_p = \frac{r_p}{R_p}, \qquad \tilde{r}_o = \frac{r_o}{R_p}, \qquad \tau = \frac{t}{\theta}, \qquad \theta = \frac{R_p}{\beta_p c_S^{n_2}},$$
$$\tilde{c}_1 = \frac{c_1}{c_S}, \qquad \tilde{c}_2 = \frac{c_2}{c_S}, \tag{35}$$

$$\tilde{n}_o(\tilde{r}_o, \tau) = n_o(r_o R_p, t\theta)\frac{R_p}{N_p},$$
$$\tilde{\nu}(\tilde{r}_o, \tilde{r}_p) = \nu(r_o R_p, r_p R_p) R_p^4, \tag{36}$$

$$\beta_p = \frac{k_p}{\bar{\rho}_p}, \qquad \beta_o = \frac{k_o}{\bar{\rho}_o}, \qquad \beta = \frac{\beta_o c_S^{(n_1 - n_2)}}{\beta_p},$$
$$c_S = \frac{N_p \bar{\rho}_o V_o^0}{V}, \tag{37}$$

the "homogeneous" sporulation model developed in Section 4 (uniform ensemble of ore particles and constant particle density ρ_p) attains the form:

$$\frac{d\tilde{r}_p}{d\tau} = -[\tilde{c}_2(\tau)]^{n_2}, \qquad \tilde{r}_p(0) = 1, \tag{38}$$

$$\frac{\partial \tilde{n}_o}{\partial \tau} = \beta\,[\tilde{c}_1(\tau)]^{n_1}\frac{\partial \tilde{n}_o}{\partial \tilde{r}_o} + [\tilde{c}_2(\tau)]^{n_2} 4\pi \tilde{r}_p^2 \tilde{\nu}(\tilde{r}_o, \tilde{r}_p),$$
$$\tilde{n}_o(\tilde{r}_o, 0) = 0, \tag{39}$$

where the dimensionless distribution $\tilde{\nu}(\tilde{r}_o, \tilde{r}_p)$ satisfies the integral constraint:

$$\int_0^{\tilde{r}_p} \tilde{\nu}(\tilde{r}_o, \tilde{r}_p)\frac{4}{3}\pi \tilde{r}_o^3\, d\tilde{r}_o = \frac{\rho_p - \rho_g}{\rho_o - \rho_g}. \tag{40}$$

According to the reaction scheme Eqs. (32) and (33), the fluid reactant concentrations $\tilde{c}_1$ and $\tilde{c}_2$ can be expressed with respect to the conversions $X(\tau)$, $Y(\tau)$ as:

$$\tilde{c}_1(\tau) = \tilde{c}_1(0) - \nu_1 X(\tau), \tag{41}$$

$$\tilde{c}_2(\tau) = \tilde{c}_2(0) - \nu_2 X(\tau) - \tilde{\mu}_2 Y(\tau), \tag{42}$$

where

$$X(\tau) = 1 - \tilde{r}_p^3(\tau) - \frac{\int_0^1 \tilde{n}_o(\tilde{r}_o, \tau)(4/3)\pi \tilde{r}_o^3\, d\tilde{r}_o}{V_o^0}, \tag{43}$$

$$Y(\tau) = 1 - \tilde{r}_p^3(t), \tag{44}$$

$$\tilde{\mu}_2 = \frac{\bar{\rho}_g}{\bar{\rho}_o}\left(\frac{V_p^0}{V_o^0} - 1\right), \tag{45}$$

$$\frac{V_o^0}{V_p^0} = \frac{\int_0^1 4\pi(\tilde{r}'_p)^2\, d\tilde{r}'_p \int_0^{\tilde{r}'_p} \tilde{\nu}(\tilde{r}_o, \tilde{r}'_p)(4/3)\pi \tilde{r}_o^3\, d\tilde{r}_o}{(4/3)\pi}$$
$$= \frac{\rho_p - \rho_g}{\rho_o - \rho_g}. \tag{46}$$

The stoichiometric loading conditions for fluid reactants $\tilde{c}_1(0)$ and $\tilde{c}_2(0)$ (for a complete dissolution of the solid matrix and of oxide grains) read as:

$$\tilde{c}_1(0) \geq \tilde{c}_1^{\text{stoic}} = \nu_1, \qquad \tilde{c}_2(0) \geq \tilde{c}_2^{\text{stoic}} = \nu_2 + \tilde{\mu}_2. \tag{47}$$

In order to fully specify the sporulation model, we need to define the functional form of the oxide grain distribution $\tilde{\nu}(\tilde{r}_o, \tilde{r}_p)$. In order to satisfy the integral constraint Eq. (40) we define:

$$\tilde{\nu}(\tilde{r}_o, \tilde{r}_p) = \hat{\nu}(\tilde{r}_o, \tilde{r}_p)\Gamma(\tilde{r}_p), \tag{48}$$

where $\hat{\nu}(\tilde{r}_o, \tilde{r}_p)$ could be a generic function, such as:

$$\hat{\nu}(\tilde{r}_o, \tilde{r}_p) = \begin{cases} \tilde{r}_o^{\zeta_1} \exp[-\zeta_2 \tilde{r}_o] & \\ \quad \times \exp[-\zeta_3 \tilde{r}_p](\tilde{r}_p - \tilde{r}_o), & \text{for } \tilde{r}_o < \tilde{r}_p, \\ 0, & \text{for } \tilde{r}_o \geq \tilde{r}_p, \end{cases} \tag{49}$$

and $\Gamma(\tilde{r}_p)$ is defined by the integral constraint Eq. (40):

$$\Gamma(\tilde{r}_p) = \frac{\rho_p - \rho_g}{\rho_o - \rho_g}\left[\int_0^{\tilde{r}_p} \tilde{\nu}(\tilde{r}_o, \tilde{r}_p)\frac{4}{3}\pi \tilde{r}_o^3\, d\tilde{r}_o\right]^{-1}. \tag{50}$$

The functional form Eq. (49) for $\hat{\nu}(\tilde{r}_o, \tilde{r}_p)$ is very flexible for reproducing different physical situations. In fact, the physical properties of the interparticle structure associated with the functional form of $\hat{\nu}(\tilde{r}_o, \tilde{r}_p)$ can be interpreted more conveniently by considering the quantity $m_o(\tilde{r}_o)$, which is the weight distribution function of oxide grains within the ore particle. Consequently, $m_o(\tilde{r}_o)\, d\tilde{r}_o$ represents the weight fraction of oxide grains of radius in the range $[\tilde{r}_o, \tilde{r}_o + d\tilde{r}_o]$ embedded in the ore particle at time $t = 0$. The behaviour of $m_o(\tilde{r}_o)$ is controlled by the distribution function $\tilde{\nu}(\tilde{r}_o, \tilde{r}_p)$, since:

$$m_o(\tilde{r}_o) = \frac{1}{V_o^0}\frac{4}{3}\pi \tilde{r}_o^3 \int_0^1 \tilde{\nu}(\tilde{r}_o, \tilde{r}_p) 4\pi \tilde{r}_p^2\, d\tilde{r}_p. \tag{51}$$

Fig. 5 shows the behaviour of $m_o(\tilde{r}_o)$ for the distribution $\tilde{\nu}(\tilde{r}_o, \tilde{r}_p)$ given by Eqs. (48)–(50) with $\zeta_1 = 1$, $\zeta_3 = 0$ and for different values of the parameter $\zeta_2 = 1, 10, 30, 50$, and 100. For increasing values of the parameter ζ_2, the average radius of the oxide grains moves towards lower values of $\tilde{r}_o$. This implies that, when the ore particle "sporulates" and oxide grains are released into the liquid solution, the contact

[3] The reference concentration c_S is the ratio between the total number of moles of metallic oxide S embedded in the ore particles and the volume V of the liquid mixture (supposed to be constant during the dissolution process). In other words, c_S is the maximum concentration of recovered metal P in the liquid solution that can be obtained from a complete dissolution of the ore particles and of the oxide grains.

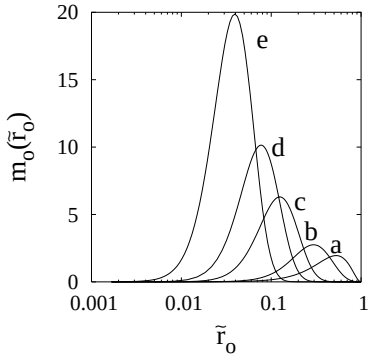

Fig. 5. Weight distribution function of oxide grains within the ore particle $m_o(\tilde{r}_o)$ for $\tilde{\nu}(\tilde{r}_o, \tilde{r}_p)$ given by Eqs. (48)–(50) with $\zeta_1 = 1$, $\zeta_3 = 0$ and for different values of the parameter ζ_2. (a) $\zeta_2 = 1$; (b) $\zeta_2 = 10$; (c) $\zeta_2 = 30$; (d) $\zeta_2 = 50$; (e) $\zeta_2 = 100$.

surface between metal oxide and liquid reactant increases for increasing values of ζ_2. The obvious consequence on the time behaviour of oxide conversion is that $X(\tau)$ exhibits a faster increase for increasing values of ζ_2 as will be shown in Section 5.1, where the response of the sporulation model is analysed in the cases of zero- and first-order kinetics for the consumption rates of the solid matrix and oxide grains.

5.1. Zero- and first-order kinetics

In the case of zero-order kinetics for the consumption rates of the solid matrix and oxide grains ($n_1 = 0$ and $n_2 = 0$), the sporulation model can be solved in closed form, thus obtaining:

$$\tilde{r}_p(\tau) = \begin{cases} 1-\tau, & 0 \le \tau < 1, \\ 0, & \tau \ge 1, \end{cases} \tag{52}$$

$$\tilde{n}_o(\tilde{r}_o, \tau) = \frac{1}{\beta}\int_{\tilde{r}_o}^{1} f(\tilde{r}'_o, \tilde{r}_p(\tau-\tau'))\eta(\tau-\tau')\,d\tilde{r}'_o,$$
$$\tau' = \frac{\tilde{r}'_o - \tilde{r}_o}{\beta}, \tag{53}$$

where

$$f(\tilde{r}_o, \tilde{r}_p(\tau)) = 4\pi\tilde{r}_p^2(\tau), \tilde{\nu}(\tilde{r}_o, \tilde{r}_p(\tau)), \tag{54}$$

$$\eta(\tau-\tau') = \begin{cases} 0, & 0 \le \tau < \tau', \\ 1, & \tau \ge \tau', \end{cases} \tag{55}$$

Fig. 6A and B show the behaviour of the conversion–time curves $(1-X(\tau))^{1/3}$ versus τ for $\beta = 0.1$ (Fig. 6 A) and $\beta = 1$ (Fig. 6B) and for three different values of the parameter $\zeta_2 = 1, 10, 100$ entering the distribution function $\tilde{\nu}(\tilde{r}_o, \tilde{r}_p)$ (Eqs. (48)–(50)). We prefer to represent the conversion–time curves as $(1-X)^{1/3}$ versus time for graphical reasons, in order to emphasise the difference with respect to the linear behaviour $(1-X(\tau))^{1/3} = \tau/\beta$ (dotted curves) characterising the classical shrinking-core model in the reaction-controlled regime (for a zero-order kinetics).

From Eq. (52), it is easy to verify that the solid matrix dissolves completely after a dimensionless time $\tau = 1$, so that, for $\tau > 1$, all oxide grains are released into the liquid solution. In the case $\beta < 1$ (the consumption of oxide grains is slower than the consumption of the solid matrix), it is more evident that the larger ζ_2 is (the smaller the average radius of oxide grains released is) and the faster the increase of the conversion is (decrease of $1-X$) at short–intermediate time-scales. For $\beta < 1$, the apparent overall reaction rate is faster than that predicted by the shrinking-core model. For $\beta = 1$, the sporulation model, at short–intermediate time-scales, exhibits an increase of the conversion X which is slower than the corresponding one in the shrinking-core model and approaches the conversion–time curve of the shrinking-core model for increasing values of ζ_2.

In the case of first-order kinetics for the consumption rates of the solid matrix and oxide grains ($n_1 = 1$ and $n_2 = 1$), the sporulation model must be solved numerically. More specifically, we adopted a classical finite-volume approach for solving the population balance Eq. (39), by discretising the oxide grain radius domain $[0, 1]$ into $N = 300$ elementary cells. The resulting system of N ODEs in the N cell

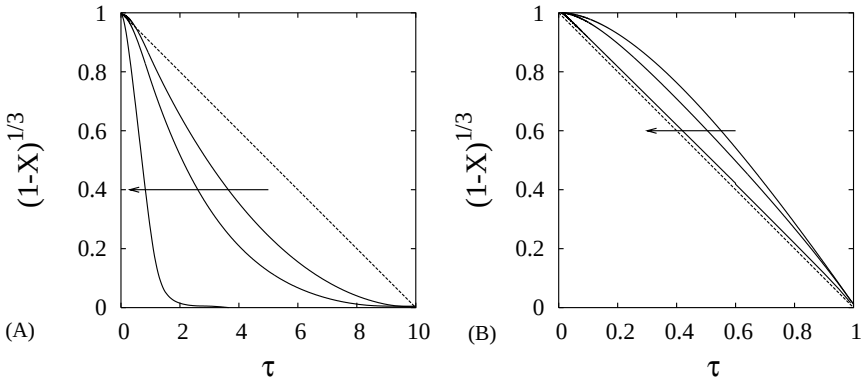

Fig. 6. Conversion–time curves $(1-X(\tau))^{1/3}$ vs. τ for the sporulation model in the presence of a zero-order kinetics ($n_1 = n_2 = 0$) (Eqs. (38) and (39)): (A) $\beta = 0.1$; (B) $\beta = 1$. Different curves correspond to different values of the parameter $\zeta_2 = 1, 10$, and 100 entering the distribution function $\tilde{\nu}(\tilde{r}_o, \tilde{r}_p)$ (Eq. (49)). $\zeta_1 = 1$, $\zeta_3 = 0$. The arrow indicates increasing values of ζ_2. The dotted line corresponds to the linear behaviour $(1-X(\tau))^{1/3} = \tau/\beta$ characterising the classical shrinking-core model in the reaction-controlled regime (for a zero-order kinetics).

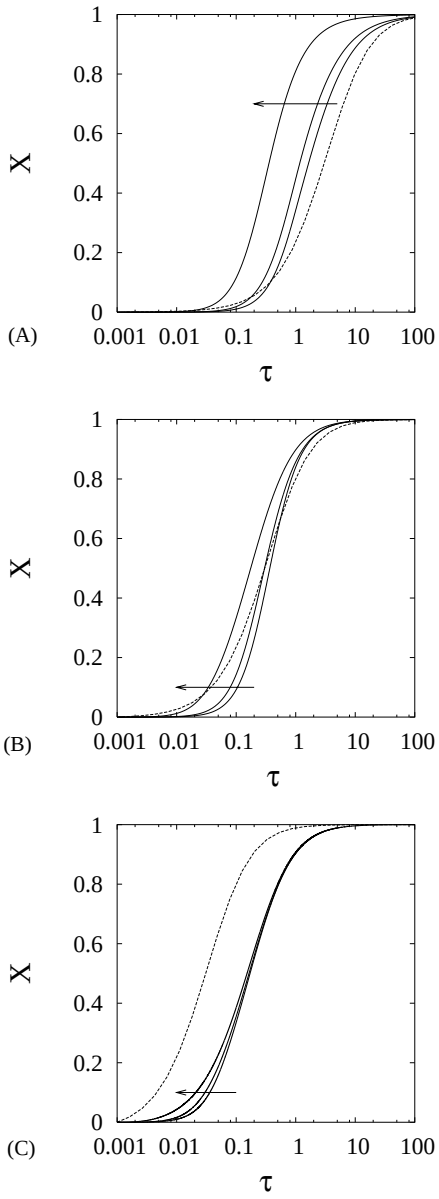

Fig. 7. Conversion–time curves $X(\tau)$ vs. τ for the sporulation model in the presence of a first-order order kinetics ($n_1 = n_2 = 1$) (Eqs. (38) and (39)) under stoichiometric loading conditions $\tilde{c}_1(0) = \nu_1$, $\tilde{c}_2(0) = \nu_2 + \tilde{\mu}_2$, ($\nu_1 = \nu_2 = \tilde{\mu}_2 = 1$). (A) $\beta = 0.1$; (B) $\beta = 1$; (C) $\beta = 10$. Different curves correspond to different values of the parameter $\zeta_2 = 1$, 10, and 100 entering the distribution function $\tilde{\nu}(\tilde{r}_o, \tilde{r}_p)$ (Eq. (49)). $\zeta_1 = 1$, $\zeta_3 = 0$. The arrow indicates increasing values of ζ_2. The dotted curve corresponds to the conversion–time curve characterising the behaviour of the classical shrinking-core model in the reaction-controlled regime (for a first-order kinetics) (Eq. (56)).

variables $\{\tilde{n}_{oi}\}_{i=1}^{N}$, ($\tilde{n}_{oi}(t) = \tilde{n}_o(\tilde{r}_{oi}, t)$, $\tilde{r}_{oi} = (i - 1/2)/N$, $i = 1, \ldots, N$) together with the ODE describing the time evolution of $\tilde{r}_p$, Eq. (38), have been integrated by means of a fourth-order Runge–Kutta algorithm.

Fig. 7A–C show the behaviour of the conversion–time curves $X(\tau)$ versus τ for $\beta = 0.1$ (Fig. 7A), $\beta = 1$ (Fig. 7B) and $\beta = 10$ (Fig. 7C), and for three different values of the parameter $\zeta_2 = 1$, 10, 100 entering the distribution function $\tilde{\nu}(\tilde{r}_o, \tilde{r}_p)$ (Eqs. (48)–(50)). The other model parameters are set to $\nu_1 = \nu_2 = \tilde{\mu}_2 = 1$. The initial concentrations of the fluid reactants A_1 and A_2 are set at the stoichiometric values $\tilde{c}_1(0) = \tilde{c}_1^{stoic} = \nu_1$ and $\tilde{c}_2(0) = \tilde{c}_2^{stoic} = \nu_2 + \tilde{\mu}_2$, in order to obtain a complete conversion of the ore particles and of the oxide grains. The dotted line corresponds to the conversion–time curve characterising the behaviour of the classical shrinking-core model in the reaction-controlled regime (for a first-order kinetics):

$$\frac{dX}{d\tau} = 3(1 - X)^{2/3}\beta(\tilde{c}_2(0) - \nu_1 X). \tag{56}$$

It can be observed that the sporulation model exhibits conversion–time behaviour which can be faster (for $\beta < 1$) or slower (for $\beta > 1$) than the corresponding one of the shrinking-core model. The influence of the parameter ζ_2, controlling the average radius of oxide grains released in the liquid solution, is more pronounced for $\beta < 1$, i.e. in the case in which the rate controlling step is the dissolution of oxide grains.

Fig. 7A–C correspond to simulation results for stoichiometric loading conditions of fluid reactants. Fig. 8 shows the influence of the initial concentration $\tilde{c}_2(0)$ of the fluid reactant A_2, which participates in the dissolution of the solid matrix. The other parameters are set to $\beta = 0.1$, $\zeta_2 = 10$. Curves (a)–(c) show the behaviour of the conversion–time curves for $\tilde{c}_2(0) = 0.5\tilde{c}_2^{stoic}$, $\tilde{c}_2(0) = 0.7\tilde{c}_2^{stoic}$ and $\tilde{c}_2(0) = 1.5\tilde{c}_2^{stoic}$, respectively. The dotted curve corresponds to stoichiometric loading conditions. It is fairly evident that, for $\tilde{c}_2(0) < \tilde{c}_2^{stoic}$, the ore particle cannot dissolve completely, so that a fraction of the oxide grains remains trapped within the unreacted core of the ore particles. As a consequence, this oxide grain fraction cannot be released into the liquid solution, and the dissolution process does not proceed to the complete conversion of the oxide.

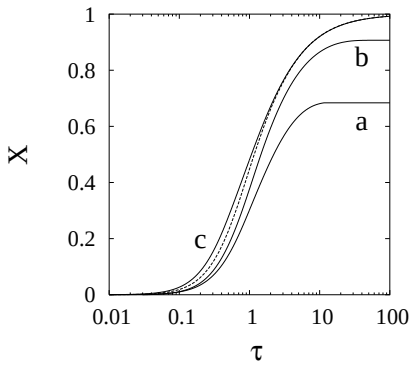

Fig. 8. Conversion–time curves $X(\tau)$ vs. τ for the sporulation model in the presence of a first-order kinetics ($n_1 = n_2 = 1$) (Eqs. (38) and (39)), for $\beta = 0.1$, $\zeta_1 = 1$, $\zeta_2 = 10$, $\zeta_3 = 0$, and for different initial concentrations $\tilde{c}_2(0)$. (a) $\tilde{c}_2(0) = 0.5\tilde{c}_2^{stoic}$; (b) $\tilde{c}_2(0) = 0.7\tilde{c}_2^{stoic}$; (c) $\tilde{c}_2(0) = 1.5\tilde{c}_2^{stoic}$. The dotted curve corresponds to stoichiometric loading conditions $\tilde{c}_1(0) = \nu_1$, $\tilde{c}_2(0) = \nu_2 + \tilde{\mu}_2$ ($\nu_1 = \nu_2 = \tilde{\mu}_2 = 1$).

6. Non-uniform radial distribution of metal oxide

In this section we formulate the sporulation model in the more general setting of a non-uniform radial distribution of metal oxide within the ore particles. In this case, the ore particle density ρ_p, and consequently the particle molar density $\bar{\rho}_p = \rho_p/MW_p$ are not constant during the dissolution process.

According to the simplified reaction scheme, Eqs. (32)–(34), the dissolution of the ore particle attains the following dimensionless form:

$$\bar{\rho}_p(\tilde{r}_p)\frac{d\tilde{r}_p}{dt} = -\beta_p(T)\left(\frac{\bar{\rho}_p^{av}(1)}{\bar{\rho}_p(\tilde{r}_p)}\right)\tilde{c}_2^{n_2},$$
$$\beta_p = \frac{k_p}{\bar{\rho}_p^{av}(1)}, \tag{57}$$

where $\bar{\rho}_p(\tilde{r}_p)$ and $\rho_p(\tilde{r}_p)$ are given by:

$$\frac{\bar{\rho}_p(\tilde{r}_p) - \bar{\rho}_g}{\bar{\rho}_o - \bar{\rho}_g} = \frac{\rho_p(\tilde{r}_p) - \rho_g}{\rho_o - \rho_g} = \int_0^{\tilde{r}_p} \frac{4}{3}\pi\tilde{r}_o^3\tilde{\nu}(\tilde{r}_o, \tilde{r}_p)\,d\tilde{r}_o, \tag{58}$$

and $\rho_p^{av}(1)$ and $\bar{\rho}_p^{av}(1)$ represent the average particle density $\rho_p^{av}(\tilde{r}_p)$ and the average particle molar density $\bar{\rho}_p^{av}(\tilde{r}_p)$, when the dimensionless ore particle radius is $\tilde{r}_p = 1$:

$$\bar{\rho}_p^{av}(\tilde{r}_p) = \frac{\int_o^{\tilde{r}_p}\bar{\rho}_p(\tilde{r}'_p)4\pi(\tilde{r}'_p)^2\,d\tilde{r}'_p}{(4/3)\pi\tilde{r}_p^3},$$
$$\rho_p^{av}(\tilde{r}_p) = \frac{\int_o^{\tilde{r}_p}\rho_p(\tilde{r}'_p)4\pi(\tilde{r}'_p)^2\,d\tilde{r}'_p}{(4/3)\pi\tilde{r}_p^3}. \tag{59}$$

The distribution $\tilde{\nu}(\tilde{r}_o, \tilde{r}_p)$ satisfies the integral constraint:

$$\frac{1}{V_p^0}\int_0^1 4\pi(\tilde{r}'_p)^2\,d\tilde{r}_p\int_0^{\tilde{r}'_p}\tilde{\nu}(\tilde{r}_o, \tilde{r}'_p)\frac{4}{3}\pi r_o^3\,dr_o$$
$$= \frac{V_o^0}{V_p^0} = \frac{\bar{\rho}_p^{av}(1) - \bar{\rho}_g}{\bar{\rho}_o - \bar{\rho}_g} = \frac{\rho_p^{av}(1) - \rho_g}{\rho_o - \rho_g}, \tag{60}$$

and controls the radial distribution of metal oxide within the ore particle.

Let us indicate with $M_o(\tilde{r}_p)$ the weight fraction of metal oxide embedded in the ore particle up to the radius $\tilde{r}_p$:

$$M_o(\tilde{r}_p) = \frac{\alpha(\tilde{r}_p)}{\alpha(1)}\tilde{r}_p^3,$$
$$\alpha(\tilde{r}_p) = \frac{\bar{\rho}_p^{av}(\tilde{r}_p) - \bar{\rho}_g}{\bar{\rho}_o - \bar{\rho}_g} = \frac{\rho_p^{av}(\tilde{r}_p) - \rho_g}{\rho_o - \rho_g}. \tag{61}$$

Fig. 9 shows the behaviour of $M_o(\tilde{r}_p)$ for:

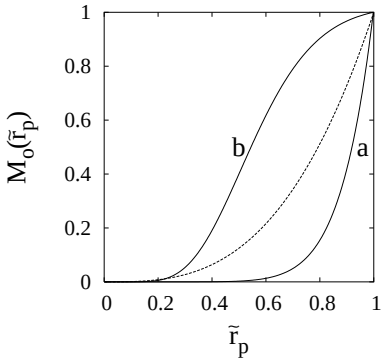

Fig. 9. Radial oxide distribution $M_o(\tilde{r}_p)$ vs. $\tilde{r}_p$ for $\tilde{\nu}(\tilde{r}_o, \tilde{r}_p)$ given by Eqs. (49) and (62) with $\zeta_1 = 1$, $\zeta_2 = 1$, and $\zeta_3 = 0$ and 15. (a) $\zeta_3 = 0$; (b) $\zeta_3 = 15$. The dotted curve $M_o(\tilde{r}_p) = \tilde{r}_p^3$ corresponds to a uniform radial distribution of metallic oxide in the ore particle.

$$\tilde{\nu}(\tilde{r}_o, \tilde{r}_p) = \hat{\nu}(\tilde{r}_o, \tilde{r}_p)\Gamma,$$
$$\Gamma = V_p^0\frac{\bar{\rho}_p^{av}(1) - \bar{\rho}_g}{\bar{\rho}_o - \bar{\rho}_g}$$
$$\times\left[\int_0^1 4\pi(\tilde{r}'_p)^2\,d\tilde{r}_p\int_0^{\tilde{r}'_p}\hat{\nu}(\tilde{r}_o, \tilde{r}'_p)\frac{4}{3}\pi r_o^3\,dr_o\right]^{-1}, \tag{62}$$

where $\hat{\nu}(\tilde{r}_o, \tilde{r}'_p)$ is given by Eq. (49) with $\zeta_1 = 1$, $\zeta_2 = 1$. Curves (a) and (b) correspond to $\zeta_3 = 0$ and $\zeta_3 = 15$, respectively. The dotted curve $M_o(\tilde{r}_p) = \tilde{r}_p^3$ corresponds to a uniform radial distribution of metallic oxide in the ore particle. It can be observed that, by letting the parameter ζ_3 vary in the range [0, 15], the model describes the localisation of the metal oxide mainly in the external part ($\zeta_3 = 0$) or in the centre ($\zeta_3 = 15$) of the ore particle.

The sporulation model, for a uniform ensemble of ore particles and a non-uniform radial distribution of metal oxide, attains the form:

$$\frac{d\tilde{r}_p}{d\tau} = -\left(\frac{\bar{\rho}_p^{av}(1)}{\bar{\rho}_p(\tilde{r}_p)}\right)[\tilde{c}_2(\tau)]^{n_2}, \qquad \tilde{r}_p(0) = 1, \tag{63}$$

$$\frac{\partial\tilde{n}_o}{\partial\tau} = \beta[\tilde{c}_1(\tau)]^{n_1}\frac{\partial\tilde{n}_o}{\partial\tilde{r}_o} + \left(\frac{\bar{\rho}_p^{av}(1)}{\bar{\rho}_p(\tilde{r}_p)}\right)[\tilde{c}_2(\tau)]^{n_2}4\pi\tilde{r}_p^2\,\tilde{\nu}(\tilde{r}_o, \tilde{r}_p),$$
$$\tilde{n}_o(\tilde{r}_o, 0) = 0, \tag{64}$$

$$\tilde{c}_1(\tau) = \tilde{c}_1(0) - \nu_1 X(\tau), \tag{65}$$

$$\tilde{c}_2(\tau) = \tilde{c}_2(0) - \nu_2 X(\tau) - \tilde{\mu}_2 Y(\tau), \tag{66}$$

where

$$X(\tau) = 1 - \left(\frac{\alpha(\tilde{r}_p)}{\alpha(1)}\right)\tilde{r}_p^3(\tau) - \frac{\int_0^1\tilde{n}_o(\tilde{r}_o, \tau)\frac{4}{3}\pi\tilde{r}_o^3 d\tilde{r}_o}{V_o^0}, \tag{67}$$

$$Y(\tau) = 1 - \tilde{r}_p^3(t)\left(\frac{1 - \alpha(\tilde{r}_p)}{1 - \alpha(1)}\right), \tag{68}$$

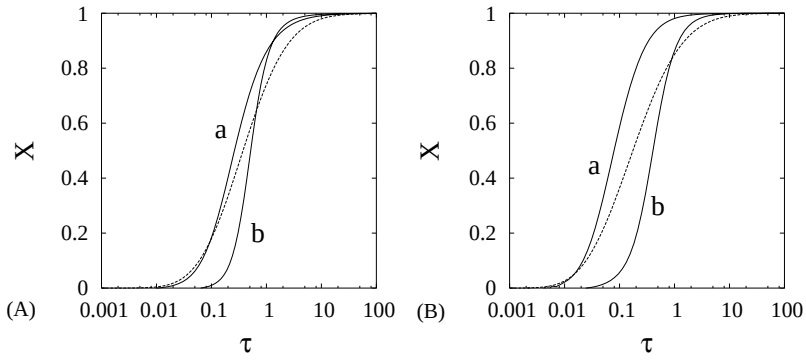

Fig. 10. Conversion–time curves $X(\tau)$ vs. τ for the sporulation model Eqs. (63) and (64) for $n_1 = n_2 = 1$, under stoichiometric loading conditions $\tilde{c}_1(0) = \nu_1$, $\tilde{c}_2(0) = \nu_2 + \tilde{\mu}_2$ ($\nu_1 = \nu_2 = \tilde{\mu}_2 = 1$). The distribution $\tilde{\nu}(\tilde{r}_o, \tilde{r}_p)$ is given by Eqs. (49) and (62) with $\zeta_1 = 1$, $\zeta_2 = 1$, and $\zeta_3 = 0$ and 15. (A) $\beta = 1$; (B) $\beta = 10$. Curves (a) and (b) correspond to $\zeta_3 = 0$ and 15, respectively. Curves (a) and (b) are associated with the radial oxide distributions $M_o(\tilde{r}_p)$ curves (a) and (b) in Fig. 8. The dotted lines correspond to the conversion–time curves $X(\tau)$ vs. τ obtained for a uniform ensemble of ore particles characterised by a uniform radial distribution of metal oxide and such that the (constant) density ρ_p equals the initial average density $\rho_p^{av}(1)$ of the ore particles.

$$\tilde{\mu}_2 = \frac{\bar{\rho}_g}{\bar{\rho}_o}\left(\frac{V_p^0}{V_o^0} - 1\right) = \frac{\bar{\rho}_g}{\bar{\rho}_o}\left(\frac{1}{\alpha(1)} - 1\right), \tag{69}$$

where $\alpha(\tilde{r}_p)$ is defined by Eq. (61).

Fig. 10 shows the behaviour of the conversion–time curves $X(\tau)$ versus τ obtained from the numerical integration of the sporulation model Eqs. (63) and (64) for $n_1 = n_2 = 1$, under stoichiometric loading conditions. The distribution $\tilde{\nu}(\tilde{r}_o, \tilde{r}_p)$ is given by Eqs. (49)–(62) with $\zeta_1 = 1$, $\zeta_2 = 1$, and $\zeta_3 = 0, 15$. Fig. 10A and B corresponds to $\beta = 1$ and 10, respectively. Curves (a) and (b) refer to $\zeta_3 = 0$ and 15, respectively (curves (a) and (b) are associated with the radial oxide distributions $M_o(\tilde{r}_p)$ (a) and (b) depicted in Fig. 9). The dotted lines correspond to the conversion–time curves $X(\tau)$ versus τ obtained for a uniform ensemble of ore particles characterised by a uniform radial distribution of metal oxide (see Section 5) and such that the (constant) density ρ_p equals the initial average density $\rho_p^{av}(1)$ of the ore particles, i.e. $(\rho_p - \rho_g)/(\rho_o - \rho_g) = (\rho_p^{av}(1) - \rho_g)/(\rho_o - \rho_g) = \alpha(1)$.

As expected, the conversion X, at short–intermediate time-scales, exhibits a faster or a slower increase (with respect to the conversion–time curve for a uniform radial distribution) depending on the value of ζ_3: slower for $\zeta_3 = 15$ (metal oxide is mainly concentrated within the inner core of the particle), and faster for $\zeta_3 = 0$ (metal oxide is mainly localised in the external shell) This effect is more pronounced for values of $\beta > 1$ when the dissolution of oxide grains is faster than the dissolution of the solid matrix (representing the rate controlling step).

7. Analysis of manganiferous ore kinetics

We applied the sporulation model to interpret the dissolution kinetics of manganiferous ores, discussed in Section 3. The experimental data depicted in Fig. 2A–C clearly indicate that sulphuric acid acts as a fluid reactant for the dissolution of both oxide grains and solid matrix. As discussed in Section 3, experimental data for pure MnO_2 particles (Fig. 1), that the dissolution rate of oxide grain is independent of sulphuric acid concentration. Therefore, the reaction scheme is the same as that considered in Section 5, Eqs. (32)–(34), where A_1 = glucose, A_2 = sulphuric acid. From the overall stoichiometry Eq. (7), we have $\nu_1 = 1/12$, $\nu_2 = 1$, while the kinetic analysis of pure MnO_2 particle dissolution Eq. (8) suggests $n_1 = 1.2$. The stoichiometric coefficient μ_2 and the kinetic parameter n_2 entering the model must be determined from the analysis of the dissolution kinetics of manganiferous ores.

From granulometric data reported in Fig. 3A–C, we may reasonably assume that: (i) the initial mixture of ore particle (Fig. 3A) can be modelled as a uniform ensemble of ore particles of radius $R_p \simeq 150\,\mu m$; and (ii) the average radius r_o of oxide grains (embedded in the ore particle and subsequently released in the liquid solution) is two orders of magnitude smaller than R_p, that is $r_o/R_p \in [0.01, 0.03]$. The latter information is extremely useful for setting the functional form and fixing the parameter value characterising the distribution function $\nu(r_o, r_p)$. We adopted the "homogeneous" sporulation model (uniform ensemble of ore particles and uniform radial distribution of metal oxide within the ore particle), Eqs. (38) and (39), and the distribution $\tilde{\nu}(\tilde{r}_o, \tilde{r}_p)$ is given by Eqs. (48)–(50) with $\zeta_1 = 0$, $\zeta_3 = 0$ and $\zeta_2 = 100$ (see Fig. 5, curve (e), for the corresponding behaviour of the weight distribution function $m_o(\tilde{r}_o)$, showing that the average radius of oxide grains is two orders of magnitude smaller than the ore particle radius).

The parameters that need to be determined from the analysis of experimental data are $\theta(T)$ (the characteristic time used in the definition of the dimensionless time τ) which is a function of the temperature T, $\beta(T)$, $\tilde{\mu}_2$ and n_2.

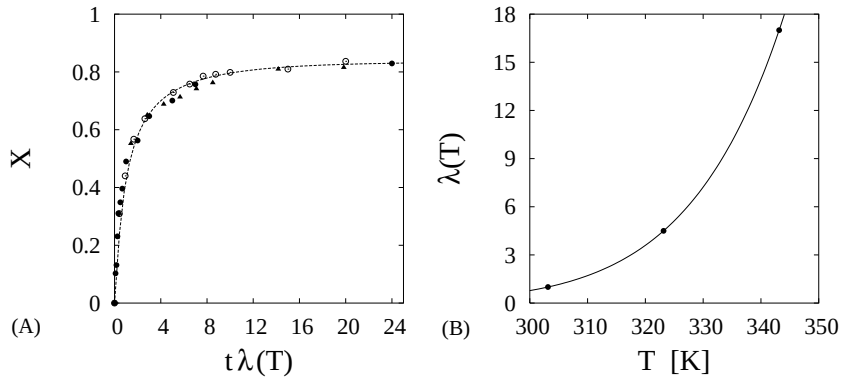

Fig. 11. (A) Conversion–time curves $X(t)$ vs. the rescaled time $t\lambda(T)$ for $T = 30^{\circ}$C (●), $T = 50^{\circ}$C (○) and $T = 70^{\circ}$C (▲). The loading conditions are $\tilde{c}_1(0) = \nu_1$ and $\tilde{c}_2(0) = \nu_2$. (B) $\lambda(T)$ vs. T (K) for $T \in [30, 70]\,^{\circ}$C. The continuous line represents the Arrhenius-type behaviour (Eq. (70)), with $E/R = 7368.2$ K and λ_o is such that $\lambda(30\,^{\circ}\text{C}) = 1$.

A preliminary analysis of the experimental data reported in Fig. 2A shows that the conversion–time curves for $T = 30^{\circ}$C (●, curve (a)), $T = 50\,^{\circ}$C (○, curve (b)) and $T = 70\,^{\circ}$C (▲), curve (c)) can be rescaled onto a unique invariant master curve (see Fig. 11A) by introducing the rescaled time $t\lambda(T)$, where $\lambda(T)$ exhibits the classical Arrhenius-type behaviour:

$$\lambda(T) = \lambda_o \exp\left(-\frac{E}{RT}\right), \tag{70}$$

depicted in Fig. 11B.

This observation has two important consequences: (i) the characteristic time $\theta(T)$ can be expressed as $\theta(T) = \theta_o/\lambda(T)$; and (ii) the kinetic parameter β is independent of temperature. By considering that $\beta \sim \beta_o(T)/\beta_p(T) \sim k_o(T)/k_p(T)$, the fact that β is independent of temperature implies that the Arrhenius-type dependence of the kinetic constants k_p and k_o on the temperature is characterised by the same activation energy E.

Fig. 2A shows the excellent agreement between experimental data and the sporulation model (continuous lines) with $n_2 = 1$, $\tilde{\mu}_2 = 1$ and $\beta = 0.043$, $\theta_o = 8$ min. It is not surprising that $\beta \ll 1$, because the short–intermediate time-scale decay of the conversion, in the case of manganiferous ores, is significantly faster than the corresponding one in the case of pure MnO_2 particles (when the classical shrinking-core model more reasonably applies). Moreover $\tilde{\mu}_2 = 1$ clearly explains why, for $\tilde{c}_2(0) = \nu_2$, the conversion saturates towards a limiting value X_s. Indeed, $\tilde{c}_2(0) = \nu_2 \ll \tilde{c}_2^{\text{stoic}} = \nu_2 + \tilde{\mu}_2$ and the sulphuric acid is a limiting reactant.

The "homogeneous" sporulation model is capable of a quantitative prediction of the influence of a surplus of sulphuric acid (see Fig. 2B) and of glucose (see Fig. 2C) in all the temperature range $T \in [30, 70]\,^{\circ}$C. Fig. 2B shows the excellent agreement between model predictions (continuous lines) and experimental data for $T = 30$, 50, 70 °C, $\tilde{c}_2(0) = 1.3\nu_2$ and $\tilde{c}_1(0) = \nu_1$. Fig. 2C shows the excellent agreement between model predictions (continuous lines) and experimental data for $T = 30$ and 70 °C, $\tilde{c}_1(0) = 1.3\nu_1$ and $\tilde{c}_2(0) = \nu_2$. Dotted curves and open circles represent model predictions and experimental data, respectively, for stoichiometric loading conditions for glucose.

8. Concluding remarks

The sporulation model is a versatile structural model specifically suited to describing the dissolution kinetic in leaching processes involving non-porous ore particles. It accounts explicitly for intraparticle heterogeneity by describing the interplay between the dissolution kinetics of the main solid reactant (e.g. metal oxide) and the dissolution/fragmentation of the solid matrix (gangue). The core of the model is the choice of the grain distribution $\nu(r_o, r_p)$ which controls the average particle radius of the released oxide grains and the radial distribution of metal oxide within the particle.

The "homogeneous" sporulation model, developed for a uniform ensemble of ore particles and constant particle density, has been successfully applied to the analysis of dissolution kinetics of manganiferous ore particles which differs significantly from the dissolution kinetics of pure MnO_2 particles.

The sporulation model can be easily generalised to include the effect of polydispersity of the solid mixture, of the ore particle fragmentation (see Section 4) and of a non-uniform radial distribution of solid reactant within the ore particle (see Section 6).

References

[1] B.F. Edwards, M. Cai, H. Han, Rate equation and scaling for fragmentation with mass loss, Phys. Rev. A 41 (1990) 5755.
[2] M. Cai, B.F. Edwards, H. Han, Exact and asymptotic scaling solutions for fragmentation with mass loss, Phys. Rev. A 43 (1991) 656.
[3] M. Sahimi, Applications of Percolation Theory, Taylor & Francis, London, 1994.

[4] P.M. Adler, Porous Media. Geometry and Transports, Butterworths–Heinemann Series in Chemical Engineering, Boston, 1992.
[5] A. Velardo, M. Giona, A. Adrover, F. Pagnanelli, L. Toro, Two-layer shrinking-core model: parameter estimation for the reaction order in leaching processes, Chem. Eng. J. 90 (2002) 231.
[6] S.E. Le Blanc, H.S. Fogler, Population balance modeling of the dissolution of polydisperse solids: rate limiting regimes, AIChE J. 33 (1987) 54.
[7] S.E. Le Blanc, H.S. Fogler, Dissolution of powdered minerals: the effect of polydispersity, AIChE J. 35 (1989) 865.
[8] M. Giona, A. Adrover, F. Pagnanelli, L. Toro, A closed-form solution of population-balance models for the dissolution of polydisperse mixtures, Chem. Eng. J. 87 (2002) 275.
[9] J. Szekely, J.W. Evans, H.Y. Sohn, Gas–Solid Reactions, Academic Press, New York, 1976.
[10] J.Y. Park, O. Levenspiel, The crackling core model for the reaction of solid particles, Chem. Eng. Sci. 30 (1975) 1207.
[11] J.Y. Park, O. Levenspiel, The crackling core model for the multistep reaction of solid particles, Chem. Eng. Sci. 32 (1977) 233.
[12] J.E. Sepulveda, J.A. Herbst, A population balance approach to the modelling of multistage continuous leaching systems, AIChE Symp. Ser. 57 (1978) 41.
[13] W.W. Stange, R.P. King, L. Woollacott, Towards more effective simulation of CIP and CIL processes. 2. A population-balance-based simulation approach, J. S. Afr. Inst. Miner. Metall. 90 (1990) 307.
[14] F.K. Crundwell, A.W. Bryson, The modelling of particulate leaching reactors—the population balance approach, Hydrometallurgy 29 (1992) 275.
[15] D. Ramkrishna, The status of population balances, Rev. Chem. Eng. 3 (1985) 59.
[16] P.J. Hill, K.M. Ng, Statistics of multiple-particle breakage, AIChE J. 2 (1996) 1600.
[17] T. Kai, Y.I. Suenaga, A. Migita, T. Takahashi, Kinetic model for the simultaneous leaching of zinc sulfide and manganese dioxide in the presence of iron-oxidizing bacteria, Chem. Eng. Sci. 55 (2000) 3429.
[18] F. Veglió, F. Beolchini, A. Nardini, L. Toro, Bioleaching of pyrrhotite ore by sulfoxidans strain: kinetic analysis, Chem. Eng. Sci. 55 (2000) 783.
[19] Z. Ma, C. Ek, Rate processes and mathematical modelization of the acid leaching of a manganese carbonate ore, Hydrometallurgy 27 (1991) 125.
[20] Z. Ma, C. Ek, Engineering application of the acid leaching kinetics of a manganese carbonate ore, Hydrometallurgy 28 (1992) 223.
[21] F. Veglió, L. Toro, Reductive leaching of a concentrate manganese dioxide ore in acid solution: stoichiometry and preliminary kinetic analysis, Int. J. Miner. Process. 40 (1994) 257.
[22] M.I. Brittan, Variable activation energy model for leaching kinetics, Int. J. Miner. Process. 2 (1975) 321.
[23] F. Veglió, M. Trifoni, F. Pagnanelli, L. Toro, Shrinking core model with variable activation energy: a kinetic model of manganiferous ore leaching with sulphuric acid and lactose, Hydrometallurgy 60 (2001) 167.
[24] M. Trifoni, F. Vegliò, G. Taglieri, L. Toro, Acid leaching process by using glucose as reducing agent: a comparison among the efficiency of different kinds of manganiferous ores, Miner. Eng. 13 (2000) 217.